Electronic Supplementary Material (ESI) for Nanoscale.

Supporting Information:

Soft Cellulose II Nanospheres: Sol-Gel Behavior, Swelling and Material Synthesis

Marco Beaumont,[a,b*] Sabine Rosenfeldt,[c] Blaise L. Tardy,[b] Claudia Gusenbauer,[d] Alexey Khakalo,[e] Nonappa,[b] Martina Opietnik,[f] Antje Potthast,[a] Orlando J. Rojas,[b] Thomas Rosenau[a,g*]

[a] Department of Chemistry, Institute of Chemistry for Renewable Resources, University of Natural Resources and Life Sciences Vienna (BOKU), Konrad-Lorenz-Straße 24, A-3430 Tulln, Austria.

[b] Department of Bioproducts and Biosystems, School of Chemical Engineering, Aalto University, FI-00076 Aalto, Finland.

[c] Bavarian Polymer Institute and Department of Chemistry, University of Bayreuth, D-95440 Bayreuth, Germany.

[d] Department of Material Sciences and Process Engineering, Institute of Wood Technology and Renewable Materials, University of Natural Resources and Life Sciences (BOKU), Konrad-Lorenz-Straße 24, A-3430 Tulln, Austria.

[e] VTT - Technical Research Centre of Finland, Tietotie 4E, P.O. Box 1000, FI-02044 Espoo, Finland.

[f] Lenzing AG, Werkstraße 2, 4860 Lenzing, Austria.

[g] Johan Gadolin Process Chemistry Centre, Åbo Akademi University, Porthansgatan 3, Åbo/Turku FI-20500, Finland

*Corresponding authors:

Prof. Dr. Dr. Thomas Rosenau, thomas.rosenau@boku.ac.at

Dr. Marco Beaumont, marcobeaumont1@gmail.com

Table of contents

I. Figures and tables

Figure S1: Top: Solid-state NMR spectra of NPan in comparison to the cellulose II precursor (starting material). Inset: infrared (FTIR) spectra of NPan. Bottom: Calibration curve to determine the degree of substitution of the carboxymethylated sample. The curve is based on values from a previous publication[1].

Table S1: Crystallinity and zeta potential of NPan in comparison to the cellulose II starting material.

Figure S2: Effect of the number of passes through a microfluidizer on z-average particle size of NPan (A). pH dependency of the zeta potential of NPan (B). Effect of particle concentration (C), ionic strength (D) and phosphate buffer (E) on z-average and number-average particle size. Effect of ionic strength on the electrophoretic mobility of NPan and hard, rod-like nanocrystals (F).

Figure S3: Small-angle x-ray scattering (SAXS) on NPan.

Figure S4: AFM images of NPan on a positive, PEI-treated silicon wafer (A) and NPan on a negative silicon wafer (B). In the case of A, particles are individualized but also aggregated structures are observed, while in the case of B the particles spread and flatten (see insets). Cryo-TEM micrographs of individual NPan (C) and of NPan aggregates (minor species) (D).

Figure S5: Comparison of swelling behavior of native cellulose nanofibrils and NPan.

Figure S6: Frequency dependency of the loss tangent (tan(δ)) at different solid contents of NPan.

Figure S7: Reversible gelation of NPan under acidic condition (A). AFM topography of NPan film (B).

II. Small angle x-ray scattering (SAXS)

III. References

I. Figures and tables

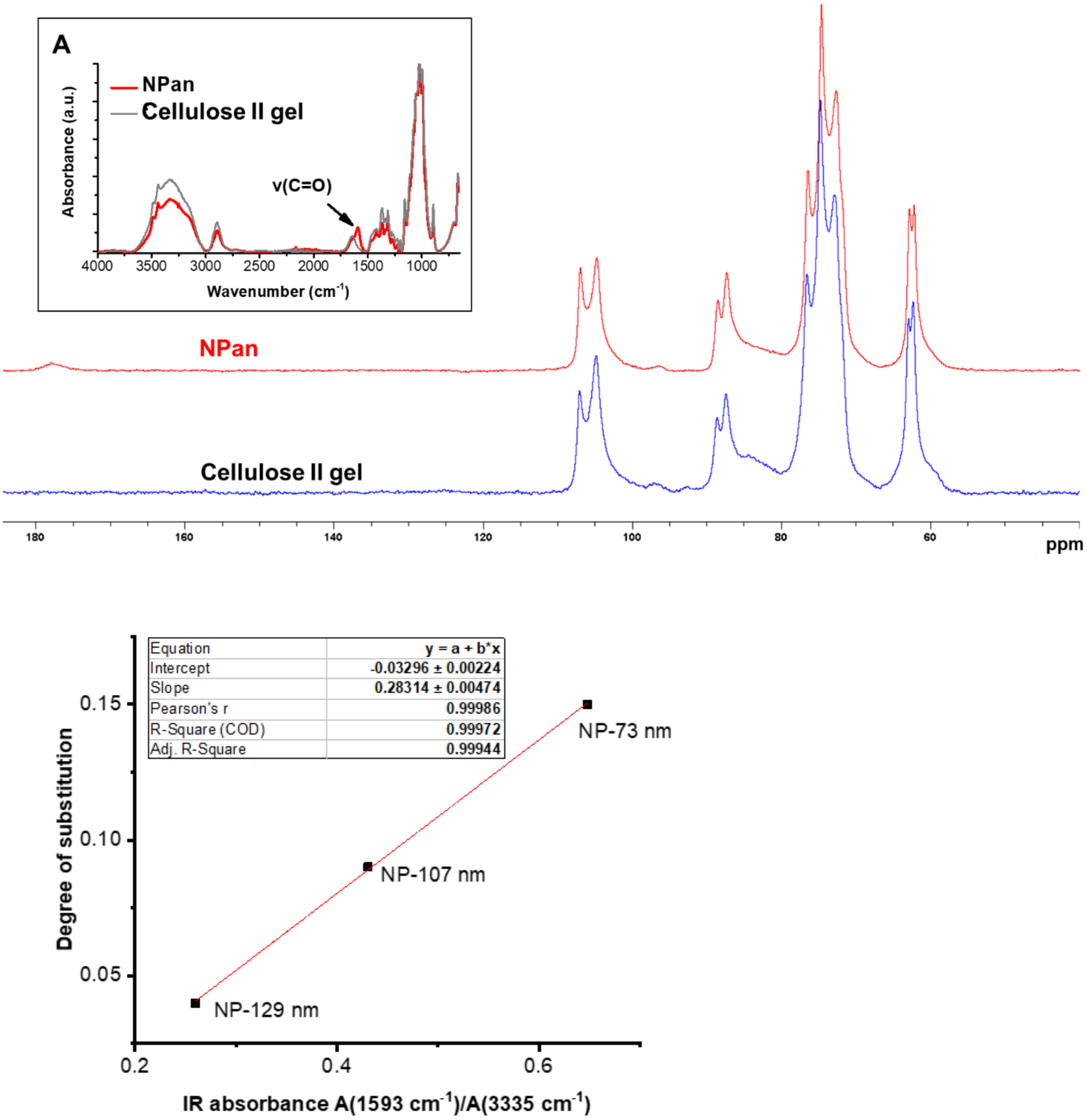

Figure S1: Top: Solid-state NMR spectra of NPan in comparison to the cellulose II precursor (starting material). Inset: infrared (FTIR) spectra of NPan. Bottom: Calibration curve to determine the degree of substitution of the carboxymethylated sample. The curve is based on values from a previous publication[1].

Table S1: Crystallinity and zeta potential of NPan in comparison to the cellulose II starting material.

	Crystallinity (NMR) / %	Zeta potential / mV	Crystallite size, D_{110} / nm
Cellulose II gel precursor	47	-	5.1
NPan	49	-30.4±2.4 (2.5 mM NaCl)	-

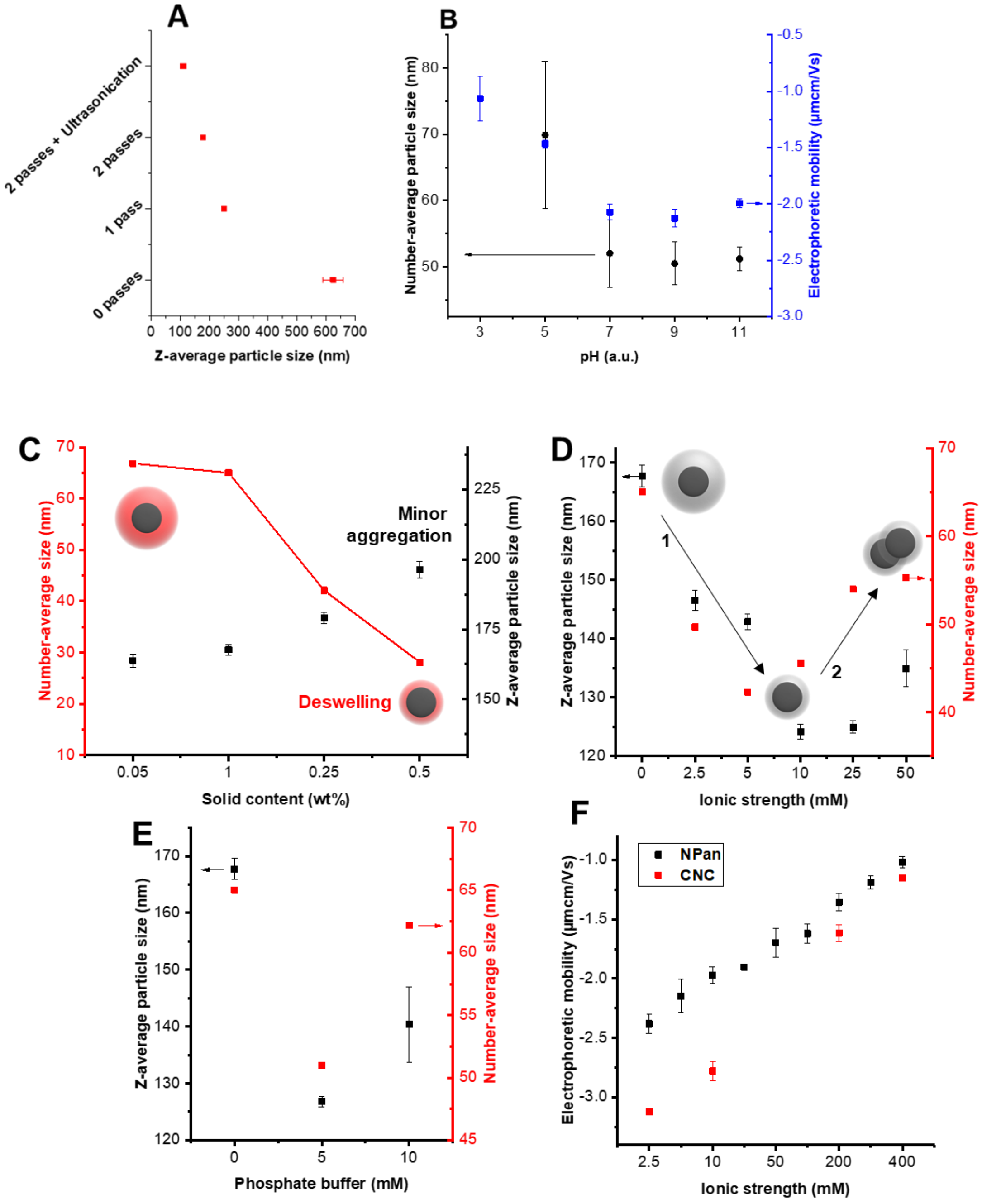

Figure S2: Effect of the number of passes through a microfluidizer on z-average particle size of NPan (A). pH dependency of the zeta potential of NPan (B). Effect of particle concentration (C), ionic strength (D) and phosphate buffer (E) on z-average and number-average particle size. Effect of ionic strength on the electrophoretic mobility of NPan in comparison to hard, rod-like nanocrystals (F).

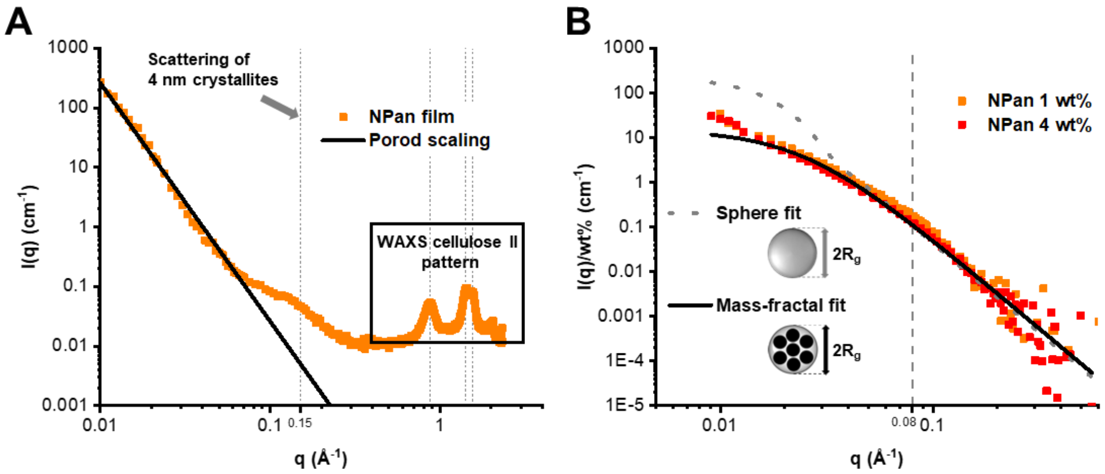

Figure S3: Small-angle x-ray scattering (SAXS) on Npan. A) Dried film (100 wt%, orange squares) with Porod scaling law indicated by the black line. The dotted lines mark prominent regions as discussed below. The X-rays passed the film in parallel geometry. Thus, SAXS is sensitive to the sheet-like structure as seen in SEM (Figure 5B1). B) Suspensions with 1 wt% (orange squares) and 4 wt% (red squares) compared to theoretical intensities (lines). The calculated intensities are based on the models of (i) a homogeneous sphere with radius R_g = 10±3 nm (Gaussian distribution, grey dotted line), (ii) a mass fractal with a radius of gyration R_g = 10 nm and a fractal dimension of D_m = 3 (black line, model for NPan core). The inset shows a sketch of the two different models. The SAXS results are further discussed at the end of the supporting information.

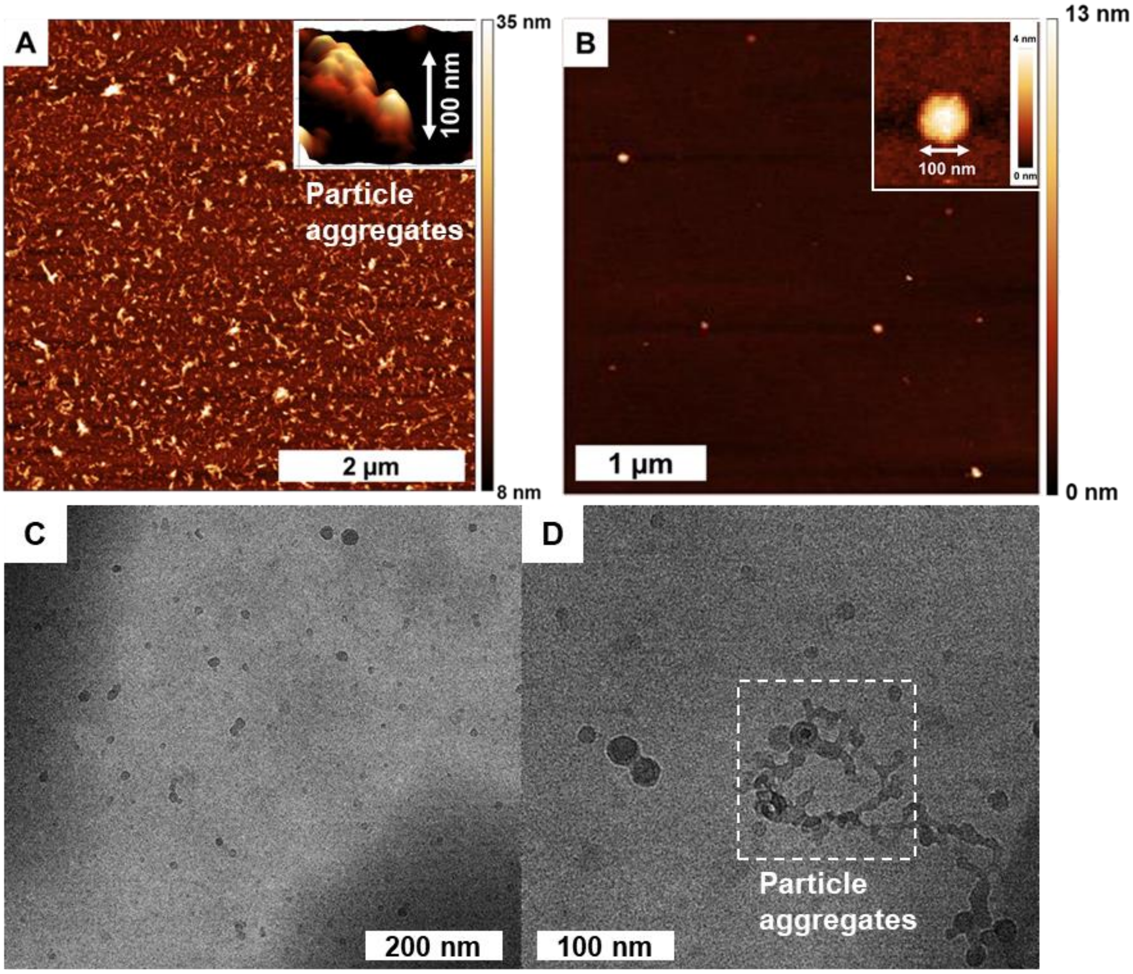

Figure S4: AFM images of NPan on positive, PEI-treated, silicon wafer (A) and NPan on a negative silicon wafer (B). In the case of A, particles are individualized but also aggregated structures are observed, while in the case of B the particles collapse and flatten (see insets). The height of the flattened particle approximates the crystallite size of NPan (B). Cryo-TEM micrographs of individual NPan (C) and of NPan aggregates (minor species) (D).

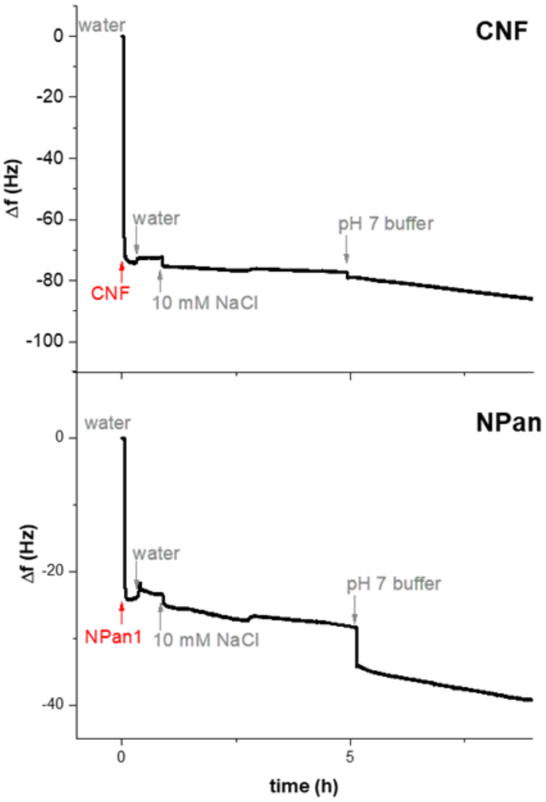

Figure S5: Comparison of swelling behavior of native cellulose nanofibrils and NPan. The behavior was studied by quartz crystal microbalance (QCM) in 10 mM NaCl and 10 mM phosphate buffer at pH 7. The influences of the buffer composition is more pronounced in the case of NPan.

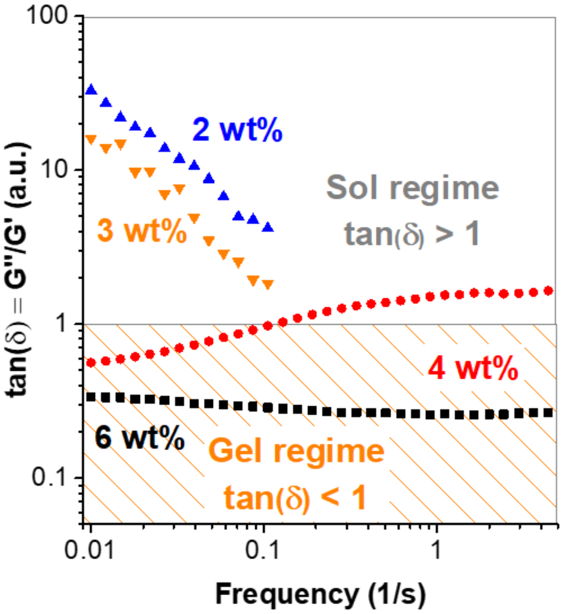

Figure S6: Frequency dependency of the loss tangent (tan(δ)) at different solid contents of NPan.

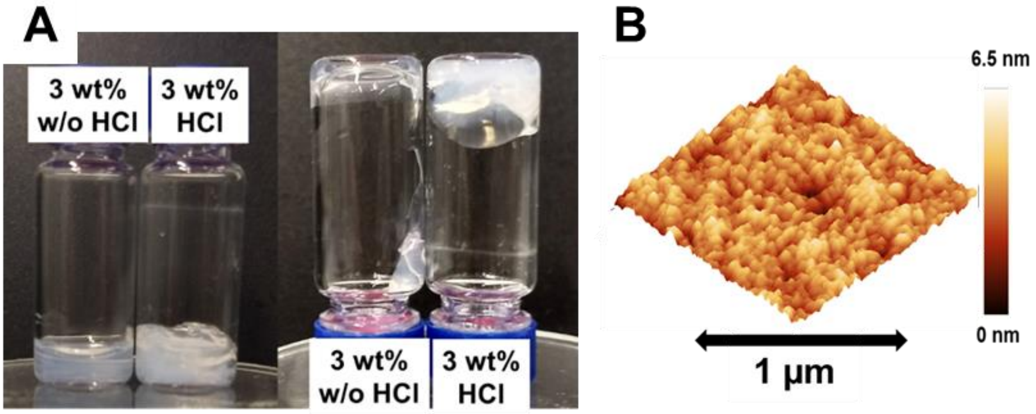

Figure S7: Reversible gelation of NPan under acidic condition (A). AFM topography of NPan film (B).

II. Small angle x-ray scattering

In **Figure 1** the small-angle x-ray scattering pattern of a NPan film, which was dried under ambient conditions, is shown. In **Figure S3A** the corresponding 1D-SAXS intensity is plotted. The data exhibit a q^{-4} power law at low q (black line), a wide shoulder around q =0.15 Å^{-1} and pronounced Bragg reflexes at high q. The peak maxima of Bragg reflexes (dotted lines at high q) result from the crystal lattice planes of the NPan and appear at the values expected for cellulose II. A correlation distance of $\frac{2\pi}{q} \approx 4$ nm (crystallite size, **Table S1** and AFM of collapsed particle in **Figure S4B**) explains the shoulder around q =0.15 Å^{-1}. Note that in 2D-SAXS pattern (**Figure 1**) the shoulder is clearly anisotropic. Such an anisotropic pattern is observed for lamellar sheet-like spacing and clearly hints at segregation of crystalline and amorphous regions. Indeed, SEM investigations (**Figure 6B1**) revealed the sheet-like structure of the film and AFM studies (**Figure S9**) showed the particle-like assembly in the film.

The contrast in cryo-transmission electron microscopy (cryo-TEM) and in small-angle x-ray scattering (SAXS) is determined by the excess electron density distribution $\Delta\rho$. The cryo-TEM image on the highly diluted NPan suspensions (**Figure 2a**) show spherical objects with a radius R around 10 nm. Thus, the samples at 1-4 wt% (symbols) were expected to scatter like homogeneous spheres with an averaged radius of 10 nm (Figure S3B, grey dotted line). Surprisingly, describing the experimental data by the scattering of spheres with *R*=10±3 nm (Gaussian distribution) failed due to an overestimation of the scattering contribution at low scattering vectors q ($q = \frac{4\pi}{\lambda}\sin\frac{\theta}{2}$, λ wave length, θ scattering angle).

The forward scattering intensity is proportional to $(\Delta\rho V_P)^2$, with V_P being the particle volume. The mass of a sphere $m(r)$ is proportional to the corresponding volume and consequently to r^3. Hence, the model of a homogeneous sphere seems to overestimate the homogeneity/compactness of the spherical NPan particles. In a next step, the mass of a less homogeneous NPan may be approximated by $m(r) \propto V_p(r) \propto r^{D_m}$ with $D_m \leq 3$, which is reasonable due to semi-crystallinity (crystallinity degree 49%). In a simplified view, due to segregation into amorphous and crystalline, NPan resembles a self-similar object, known as fractal (**Figure S3B** inset). The radius of gyration R_g describes the fractal size and the fractal dimension D the compactness. The perimeter of the aggregate is described by a cut-off function $h(r,\xi) = e^{-\frac{r}{\xi}}$, in which the correlation length ξ may be difficult to interpret. The scattering of a mass fractal $I(q)$ is given by

$$I(q) = \frac{(D-1)\ \sin[(D-1)\tan^{-1}(q,\xi)]}{(D-1)q\xi\ (1+q^2\xi^2)^{\frac{D-1}{2}}} \quad \text{with} \quad \xi^2 = \frac{2R_g^2}{D(D+1)}.$$

The scattering of small fractals with R_g = 10 nm and D=3 (fractal model for primary NPan particles) is plotted as black line in **Figure S3B**. It results $\xi = 4$ nm, a value equal to the expected crystallite size. The scattering intensities of the experimental data (symbols) are described very well by the model of these small fractals for *q*>0.02 Å^{-1}, but not before.

On the way from sol (isolated NPan) to isotropic gels (aggregated structure) the primary NPan particles interact to clusters. Those clusters are again self-similar objects and may be visualized as bigger mass fractals. The scattering intensity of a fractal with R_g = 100 nm, D=2.4 and $\xi = 50$ nm agrees with the experimental one at low q.

Most probably, the real system exhibits both kinds of clusters at the same time. Thus, the simulation of real systems is very complex. Nevertheless, the scattering of such a material should exhibit two distinct kinks in a log-log representation, corresponding approximately to characteristic subunits of the big (cluster of NPan, often not in the experimental q range) and the small fractal (primary particle NPan). The q range in-between determines the power law, which relates to the fractal dimension of the cluster. The experimental data seen in **Figure S3B** only show one break around 0.08 Å^{-1}, which corresponds to ca. 4 nm. We interpret our results in a way that the NPan are spherical core shell particles. The core is semi-crystalline and the shell highly accessible and amorphous. Carboxymethylation of the starting material occurs mainly in the amorphous regions (crystallinity was preserved through the process). After mechanical disintegration by microfluidization, the particles reorganize into the core shell structure, the negative carboxylate groups accumulate in the shell to minimize individual charge repulsion. At sufficiently high concentration NPan aggregates to clusters with fractal morphology (**Figure 5C**). This work benefited from the use of the SasFit 0.94.1.[2]

III. References

(1) Beaumont, M.; Nypelö, T.; König, J.; Zirbs, R.; Opietnik, M.; Potthast, A.; Rosenau, T. Synthesis of Redispersible Spherical Cellulose II Nanoparticles Decorated with Carboxylate Groups. *Green Chem.* **2016**, *18*, 1465–1468. https://doi.org/10.1039/C5GC03031E.

(2) Breßler, I.; Kohlbrecher, J.; Thünemann, A. F. SASfit: A Tool for Small-Angle Scattering Data Analysis Using a Library of Analytical Expressions. *J Appl Cryst* **2015**, *48* (5), 1587–1598. https://doi.org/10.1107/S1600576715016544.